Analysis of the current signature in a constant-volume combustion chamber

S. M. Aithal

Mathematics and Computer Science Division, Argonne National Laboratory,
9700 S. Cass Ave., Argonne, IL 60439, USA

Phone : 630-252-3164, e-mail: aithal@mcs.anl.gov

Abstract: Identifying charged species and their relative concentrations as a function of initial mixture composition, temperature, and pressure can play an important role in the diagnostics and control of combustion devices. This paper aims to identify important charged species and their temporal variation in a spark-ignited methane-air mixture using the equilibrium constant method. The equilibrium composition of twenty neutral and seven charged species ((e^-), CHO^+, H_3O^+, NO^+, OH^-, O_2^-, O) was obtained using a novel adaptation of the Newton-Raphson method for highly stiff nonlinear system of equations. A two-zone combustion model was used to study the effect of air-fuel ratio (AFR), on the temporal variation of charged species concentration. Temporal variation of the current computed from the equilibrium concentration of charged species was found to compare well with experimental data for several AFRs.

Keywords: equilibrium, Newton-Raphson, charged-species, ionization current, air-fuel ratio

Nomenclature

G	molar Gibbs free energy (J/mole)
k_p	equilibrium constant
R	universal gas constant (J/K)
T	temperature (K)

Greek Symbols

ρ	density

Abbreviations

AFR Air-Fuel Ratio

1 Introduction

Ionization in flames has long been a topic of interest (Calcote, 1957; Williams, 1973; Lu et. al 1969). The presence of charged species (electrons, positive and negative ions) in flames can be exploited for diagnostics and control in several engineering applications, such as plasma-enhanced combustion, ionization sensors in internal combustion (IC) engines, and sensing limits of flame blowouts in terrestrial and aerospace combustors (Nair et al, 2005). Understanding the relative concentrations of various charged species in combusting fuel-air mixtures can greatly aid the development of new control methodologies and diagnostic sensors. One of the simplest approaches for studying ionization in combusting mixtures is to initiate a spark in a constant-volume chamber filled with a fuel-air mixture of known composition and to measure the temporal variation of chamber pressure and ion current (see Figure 1). The spark can be initiated by bringing about an electrical breakdown in the space between two metal electrodes (as in a spark plug in IC engines). After the main spark event, a small DC bias (on the order of 200 V) can be applied across the electrodes of the spark plug to measure the temporal variation of the ionization current in the chamber. A pressure transducer can be used to measure the temporal variation of pressure in the cylinder after the main spark event. Figure 2 shows the pressure and current signature of a CH_4-air mixture in a constant volume cylinder (An, 1996). Since a stoichiometric CH_4-air mixture corresponds to an air-fuel ratio (AFR) of 17.16, AFR = 15 represents a slightly rich mixture, AFR = 17 represents a near-stoichiometric mixture, and AFRs = 20 and 24 represent fuel-lean mixtures with an equivalence ratio of 0.858 and 0.714,

respectively. Figure 2 shows that the mixture composition (AFR) has a strong impact on the peak current values, particularly for near-stoichiometric AFRs. The figure also shows that the current peak tracks the pressure peak, especially for near-stoichiometric AFRs. This correlation between the ionization current and chamber pressure can be used as a diagnostic tool to understand various combustion characteristics such as mixture composition and combustion quality. Since most gasoline engines operate with the AFR being close to stoichiometric, the correlation between peak current and peak pressure has the potential to be used for real-time control of automotive engines.

Some of the earliest experimental work in this area was conducted in 1960s and 1970s (see Clements, 1976 and references therein) and has continued to date (Anderson, 1986; Shimasaki et. al, 1993; Miyata et. al, 1993; Yoshiyama et. al, 2000; Yoshiyama, 2002; Tisch et. al, 2008, Henein et. al, 2010). While an abundance of research exists on experimental investigation into ion current measurements, relatively fewer numerical investigations seek to identify the charged species present in the combusting mixture (Saitzkoff et. al, 1996; Reinmann et. al 1997; Franke et. al 2003; Naoumov et. al, 2002; Ahmedi et. al, 2003; Ahmedi et. al, 2004; Yamashita et. al, 2009). The correlation between ionization current signature and pressure trace in combusting mixtures is of great interest in spark-ignited (SI) internal combustion engines because it can serve as a diagnostic tool with little modification to the existing setup, since the spark plug is an integral part of the SI engine. The spark plug can be used as an inexpensive substitute for pressure sensors and can thus be used to predict the temporal pressure variation (or position with respect to crank angle) during the compression and expansion strokes. Therefore, in addition to detecting misfires and knock, monitoring of the ionization current enables determination of the appropriate time for fuel injection and ignition. Given these benefits, much

of the work on ionization sensors has been in spark-ignited IC engines. Better understanding of the identities of the charged species responsible for the observed current signatures can be of potential benefit to combustor systems. For instance, it can lead to improved monitoring and control of combustion processes in gas turbines.

While several theories have been put forth to explain the shape of the ionization current (Anderson, 2002), researchers widely believe that the measured ionization current can be explained in terms of thermal and chemical ionization processes taking place during combustion (the second current peak shown in Figure 2 is believed to be caused by thermal ionization). However, the identities of the charge carriers responsible for generating the observed ionization current are not fully known. Earlier work on the origins of the observed ionization current alluded either to chemi-ions such as CHO^+ and H_3O^+ (Miyata et al, 1993) or to NO^+ (Saitzkoff et. al, 1996) as the charge carriers responsible for current flow. Ahmedi et al. (2004) discussed an extended ionization equilibrium study of a constant-volume chamber where they included alkali metals, namely, sodium and potassium, along with OH^-, CN^-, and O_2^- and with the thermal ionization of NO. They concluded that alkali metals present in air have a greater influence on the ion signal than does the thermal ionization of NO. They also reported that electron attachment processes have a strong influence on the current signal. In their study, they did not include the presence of positive ions such as H_3O^+ or CHO^+, which have been shown to be important in other studies. Furthermore, they did not include parametric studies on the influence of the initial trace species concentration of K and Na on the ion current. Their conclusion was also based on comparing the ion current signal with their equilibrium chemistry model for a single AFR. Details of all the species used in the equilibrium computations were also not discussed. Yamashita et al. (2009) discussed the mechanism for the ion current in a methane flame using

finite-rate kinetics. Six charged species—namely, HCO^+, e^-, H_3O^+, $C_2H_3O^+$, CH_3^+, and $C_3H_3^+$—were included in their work; however, NO^+ was not included.

The goal of the work reported here was to develop a fast and robust tool to conduct a detailed study of the equilibrium composition of combusting fuel-air mixtures, including all charged species identified in the literature as important contributors to ionization current. Such a study would help identify important charged species responsible for describing the current signatures in combustion mixtures. Seven charged species—namely, electrons (e^-), CHO^+, H_3O^+, NO^+, OH^-, O_2, and O^-—were included in the computations. The study focused on the experimental results in constant volume chamber filled with a methane-air mixture (reported in An (1996)) and compared the temporal variation of ionization current with experimental data for a range of AFRs. The experimental data reported in An (1996) was chosen for three main reasons: (1) a constant volume chamber is the simplest geometrical configuration as compared with engines that have a continuously changing volume; (2) the fuel used in the experiment was methane (CH_4), which is much simpler compared to fuels such as gasoline or diesel used in actual engine tests; and (3) experimental measurements for the temporal variation of cylinder pressure and current were presented for four different air-fuel ratios. The chemical equilibrium system under consideration included 27 species and 22 reactions, as shown in Table 1 and Table 2 (reactions 17 to 22 are ionic reactions). Ionic species such as CH_3^+ and $C_3H_3^+$ were not included because their equilibrium concentration under near-stoichiometric or lean conditions was negligible at temperatures close to 2500 K and pressures close to 10 atm (typical peak temperature and pressure conditions in a constant volume combustion of methane). This was confirmed by performing equilibrium calculations with an online CEA calculator (CEARUN). The temporal variation of the chamber pressure was used to compute the burned gas temperature.

The burned gas temperature was used to compute the reaction rate constants shown in Table 2 (after completion of combustion of the fuel-air mixture, the temperature of the entire volume is at the burned gas temperature corresponding to the cylinder pressure at that instant of time). Temporal variations of the equilibrium concentration of important species in the burned gas were obtained by using the equilibrium constant method. The predicted current signatures were then compared with existing experimental measurements reported for a constant-volume bomb (An, 1996).

This paper is organized as follows. Model formulation of the problem and the method of solution are discussed in Section 2. Current signatures predicted by the model and comparisons with experiments reported in An (1996) are discussed in Section 3. The paper concludes in Section 4 with a summary of the most important findings.

2 Method of solution

In this section we determine both the temporal variation of the burned gas temperature and the equilibrium constants.

2.1 Determination of temporal variation of burned gas temperature

Temporal variation of temperature was obtained from the temporal variation of measured pressure by using the procedure explained next. A simplified two-zone model (consisting of the burned and unburned zone) was used to compute the burned gas temperature. The following simplifying assumptions were used in the two-zone model used in this work.

1. The initial mixture is fully mixed and spatially homogenous.
2. No heat or mass transfer between the burned and unburned zone.

3. The contents of each zone are fully mixed and are characterized by a single pressure and temperature.
4. The burned and unburned zones are separated by a infinitesimally thin flame-front.
5. The instantaneous pressure in both the burned and unburned zones is equal to the experimentally measured pressure.

In a constant-volume bomb, the cylinder pressure rise is due only to the net heat input (energy due to fuel combustion and heat lost to the surrounding); hence the temporal variation of the burned gas fraction can be computed by using the rate of pressure rise (Heywood, 1988).

$$x_b(t) = \frac{(P(t) - P_0)}{(P_m - P_0)} \quad , \tag{1}$$

where $x_b(t)$ is the burned gas fraction at time t, $P(t)$ is the value of experimentally measured pressure at time t, P_o is the initial chamber pressure, and P_m is the maximum cylinder pressure (obtained from the experimental data). The burned gas fraction equals unity when the peak cylinder pressure is reached. The experimental values of initial cylinder pressure, temperature, and AFR can be used to determine the total initial moles of fuel, O_2, and N_2 in the cylinder using the ideal gas law. The initial cylinder pressure and temperature were 103.47 KPa (15 psia) and 300 K, respectively. Knowing the burned gas fraction, one can determine the mass of the burned and unburned zones at any instant of time. Before combustion begins, the mass of the burned gas is zero, while the mass of the unburned gas is equal to the initial cylinder mass. When the fuel-air mixture is fully burned, the cylinder consists entirely of the burned gas and equals the initial cylinder mass. The burned gas fraction can be used to compute the volume fraction of the burned gas $y_b(t)$ $(=V_b(t)/V_c)$ using the following relationship (Heywood, 1988).

$$x_b(t) = \left[1 + \frac{\rho_u}{\rho_b} \left(\frac{1}{y_b(t)} - 1 \right) \right]^{-1} \tag{2}$$

The ratio of unburned to the burned gas density (ρ_u/ρ_b) is set equal to 4, since it has been found to be true for most engine operating conditions as pointed out in (Heywood, 1988). The burned and average gas temperature can be computed from the ideal gas equation of state as shown below:

$$T_b(t) = \frac{P(t)V_b(t)}{m_b(t)R_{gb}} \qquad \text{for } t \le t_p, \tag{3}$$

$$T_a(t) = \frac{P(t)V_c}{m_i R_g} \qquad \text{for } t \le t_p, \tag{4}$$

where, the subscripts *b* represents burned gas quantities; t_p corresponds to the time when the peak pressure is reached and V_c is the total cylinder volume. After the peak cylinder pressure is reached, the mixture is fully burned implying, $m_b(t) = m_i$ for $t > t_p$, where m_i is the initial mass of the fuel-air mixture in the cylinder. For $t > t_p$ the temperature given by Eq. (3) equals the average cylinder temperature. A parametric study was conducted to assess the impact of the assumed ratio of ρ_u/ρ_b on the burned gas temperature. The temporal variation of the burned gas temperature was obtained for ρ_u/ρ_b varying between 3 and 5. The ratio of ρ_u/ρ_b affects the burned gas temperatures from small values of $x_b(t)$. From Eq. (2), it is seen that as $x_b(t)$ tends to unity, the influence of the density ratio is insignificant. It was seen that for $x_b(t) > 0.9$, the difference in burned gas temperature between $\rho_u/\rho_b = 3$ and $\rho_u/\rho_b = 5$ was less than 3%.

2.2 Determination of equilibrium constants

The detailed procedure to calculate the equilibrium rate constants for each reaction shown in Table 2 is explained in Aithal (2011). Briefly, Eq. (5) was used to compute the equilibrium reaction rate constant for each equation shown in Table 2 at a given temperature and pressure.

$$\ln k_p = \frac{-\Delta G^{\circ}(T)}{RT} \tag{5}$$

In the above equation, k_p is the equilibrium reaction rate constant, R is the universal gas constant, T is the temperature, and $\Delta G°$ is the change in the Gibbs free energy computed at the temperature, T. Table 2 also shows the values of the equilibrium constants for each reaction computed at 2500 K.

2.3 Numerical solution

The 22 nonlinear equations shown in Table 2, along with the atom conservation equations for C, H, O, and N, and a charge conservation equation were used to obtain the concentration of each of the 27 species shown in Table 1. This set of equations is a highly non-linear set of very stiff equations. Table 2 shows that the ratio of the largest to the smallest reaction rate constant is about 30 orders of magnitude. Solution of a large set of highly non-linear stiff equations is a computationally daunting task. In order to solve this non-linear stiff system of 27x27 equations, a novel adaption of the Newton-Raphson method was developed (Aithal, 2011). With this procedure, one can obtain the temporal variation of each of the species shown in Table 1 corresponding to a given temperature and pressure at a given instant of time. The equilibrium reaction rate constants were computed by using the burned gas temperature (computed using Eq. (3)) and the experimentally measured pressure.

3 Results and discussion

The governing equations described in the previous section were solved to compute the equilibrium concentration of charged species in the constant volume combustion-bomb experiments reported in An (1996). The modified form of the Newton-Raphson solver used in this work had been previously tested and validated (Aithal, 2011). Convergence at each temporal point (given temperature, pressure, and burned gas fraction) was ensured by letting the

residuals drop by 70 orders of magnitude. The typical computation time on a single core 2.53 GHz Intel Xenon was about 1 second. Figures 3 and 4 show the temporal variation of burned gas fractions and burned gas temperatures for various AFRs obtained with the procedure described above. Figure 3 shows that the burned gas fraction reaches unity, signifying complete fuel combustion corresponding to the time at which the peak cylinder pressure is reached. Since the pressure profiles for AFR = 15 and AFR = 17 are nearly identical (see Figure 2), the burned gas mass fraction for these two cases is also practically identical. Figure 4 shows that the temporal variation of the burned gas temperature for various AFRs follows the temporal variation of pressure shown in Figure 2. Figure 5 (a) and (b) show the temporal variation of the burned and average gas temperatures for AFR = 15 and AFR = 17, respectively. As expected, the burned and average gas temperatures are equal when the entire fuel-air mixture is completely burned when the peak cylinder temperature is reached. Similar characteristics are seen for other AFRs as well. Since the initial density of the burned gas is assumed to be a quarter of the unburned gas, the initial temperature of the burned gas is 1200 K, as dictated by the ideal gas equation of state. As explained earlier, the density ratio of burned to the unburned gas affects the initial rate of rise of the burned gas temperature when the burned gas fraction is small but has an insignificant effect as the burning of the fuel-air mixture nears completion.

Figure 2 (b) shows a marked change in the peak currents for AFRs = 15, 17, and 20; hence the charged species concentrations for these AFRs is discussed next. Figure 6 (a), (b) and (c) shows the temporal variation of all the charged species for AFRs = 15, 17, and 20, respectively. It is seen that the important charged species for each AFR are e^-, H_3O^+, NO^+, and OH^-. Figure 7 shows the equilibrium mole fractions of all charged species at temperatures and pressures corresponding to the peak current for AFRs = 15, 17, and 20. As with Figure 6, the mole

fractions of O_2^-, O^-, and HCO^+ are about two orders of magnitude lower than those for e^-, H_3O^+, NO^+, and OH^-.

The computed charged species number densities (proportional to the mole fractions) can be used to compute the temporal variation of current using the procedure described next. Assuming a simple cylindrical geometry for the current path in the spark gap, the current can be computed as

$$I(t) = \frac{A}{d} V \left(\sum_{j=1}^{N_C} e_j n_j \mu_j \right), \qquad (6)$$

where $I(t)$ is the instantaneous current; A is the cross-sectional area of the current channel (which in this case is taken to be 5 x 10^{-6} m^2, representative of electrode areas in a spark plug); d is the gap spacing (which is set here to the constant value of 0.8 mm, again representative of typical spark plug gaps); V is the terminal voltage (which is set equal to the constant value of 250 V, corresponding to experiments in An (1996)); and N_C is the number of different charge carriers considered in the model. The mobility of charged species j can be evaluated by using the mean free path theory (Mitchner, 1973):

$$\mu_j = \frac{e_j}{m_j \sum_{i=1}^{N} \nu_{ji}}, \qquad (7)$$

where μ_j is the mobility of species j, ν_{ji} is the collision frequency between species j and species i, m_j is the atomic or molecular mass of species j, and e_j is the charge on species j.

Figure 8 shows a comparison between current computed by using equilibrium number densities of charged species with experimental data for AFRs = 15 and 17. We note the impact of mixture composition on the peak ion current particularly for AFRs = 15 and 17. The temporal variation of pressure for AFRs = 15 and 17 are virtually identical (see Figure 2 (a)), and the peak

burned gas temperatures shown in Figure 4 for AFRs = 15 and 17 differ by less than 5%, yet there is about a 50% drop in peak current for AFR = 17 as compared with AFR = 15 (see Figure 2 (b)). Figure 8 shows that the current computed by using equilibrium mole-fractions of charged species predicts this current trend well, both qualitatively and qualitatively. Equation 6 shows that the contribution of each charged specie to the total current is proportional to the product of its number density and mobility. Figure 7 shows that for AFRs 15 and 17, the number densities of important charged species, namely, e^-, H_3O^+, NO^+, and OH^-, are within an order of magnitude. Since electrons are about 4 orders of magnitude lighter than the other charged species (H_3O^+, NO^+, and OH^-), their mobility is three to four orders of magnitude higher (see Eq. (7)). Hence, the contribution of the other charged species to the overall current is negligible. Figure 7 shows that relative magnitudes of the electron number density at the location of the current peaks for the three AFRs, namely, 15, 17, and 20, scale as the peak current values noted experimentally. Figure 8 also shows that the width of the predicted current distribution is narrower than that of the experimental data. For instance, at any given instant of time after the peak current has been reached, the current predicted by equilibrium assumptions is lower than that observed experimentally. The reason is that the equilibrium assumptions do not strictly hold at low temperatures and pressures. Equilibrium assumptions require the number densities of all species to change instantaneously with changing pressure and temperature. While this is a good assumption at high temperatures (above 2000 K), the deviation between the concentrations predicted by finite-rate and equilibrium chemistry becomes more pronounced at lower temperatures and pressures. The time rate of change of concentration of a particular species depends on the reaction rate constants of individual elementary reactions responsible for the net production of the specie. These reaction rate constants (usually expressed in Arrhenius form) are

functions of temperature that dictate the overall time required for change in concentration of a particular species. Figure 8 shows that as the temperature of the chamber drops (for $t > t_p$), the deviation between the current signals predicted by the equilibrium assumptions and experimentally observed data increases, as expected. Since the fuel-air mixture composition is characterized by the peak value of the current signal, equilibrium calculations can still provide useful information for various diagnostic and control applications.

4 Conclusions

This paper explored the use of equilibrium assumptions in analyzing the current signature in a constant volume combustion chamber. Equilibrium concentrations of 27 neutral and charged species typically encountered in combustion environments were computed by using the equilibrium constant method. The current drawn from the combustion chamber during the combustion event was assumed to comprise seven charged species: electrons (e^-), CHO^+, H_3O^+, NO^+, OH^-, O_2^-, and O^-. The temporal variation of temperature and pressure was used to compute the temporal variation of the equilibrium products in the burned zone. It was seen that the important charged species for all the AFRs studied in this work were e^-, H_3O^+, NO^+, and OH^-. The mole fractions of O_2^-, O^-, and HCO^+ were about two orders of magnitude lower than those of the important charged species at the peak current values. Temporal variation of the current computed from the equilibrium concentration of charged species was found to compare well with experimental data for several AFRs. The effect of AFR (mixture composition) on the current signature was captured well. It was seen experimentally that the mixture composition had a greater impact on the peak current as compared with temperature. This behavior was captured correctly by the equilibrium model.

Acknowledgments: This work was supported by the Office of Science, U.S. Department of Energy, under Contract No. DE-AC02-06CH11357.

References:

Ahmedi, A., Franke, A., Soyhan, H.S, Mauss, F. and Sundén, B. (2003). Prediction Tool for the Ion Current in SI Combustion. SAE Paper Number: 2003-01-3136.

Ahmedi, A., Mauss, F., and Sunden, B. (2004). Analysis of an Extended Ionization Equilibrium in the Post-Flame Gases for Spark Ignited Combustion. ASME Conf. Proc. 2004, 373.

Aithal, S.M. (2011). Equilibrium Chemistry Calculations for Lean and Rich Hydrocarbon-Air Mixtures. Preprint ANL/MCS-P1825-0111, Argonne National Laboratory, Argonne, Illinois.

An, F. (1996). Combustion Diagnostics in Methane-Fueled SI Engines Using the Spark Plug as an Ionization Probe. M.S. thesis, Department of Mechanical Engineering, The Ohio State University.

Andersson, I. (2002). Cylinder Pressure and Ionization Current Modeling for Spark Ignited Engines. Ph.D. dissertation, Linköping University.

Anderson, R.L. (1986). In-Cylinder Measurement of Combustion Characteristics Using Ionization Sensors. SAE Paper 860485.

Calcote, H.F. (1957). Mechanisms for the Formation of Ions in Flames. Combustion and Flame, 1, 385.

CEARUN, http://cearun.grc.nasa.gov/

Clements, R.M. and Smy, P. R. (1976). The Variation of Ionization with Air/Fuel Ratio for a Spark-Ignition Engine. Journal of Applied Physics, 47, 505.

Franke, A., Einewall, P., Reinmann, R. and Larsson, A. (2003). Analysis of the Ionization Equilibrium in the Post-Flame Zone. SAE Paper Number: 2003-01-0715.

Henein, N. A., Bryzik, W., Abdel-Rehim, A. and Gupta, A. (2010). Characteristics of Ion Current Signals in Compression Ignition and Spark Ignition Engines. SAE Paper Number: 2010-01-0567.

Heywood, J. B. (1988). Internal Combustion Engine Fundamentals. McGraw-Hill: New York.

Lu, P.L., Dabora, E. K. and Nicholls, J. A. (1969). The Structure of H2-CO-O2 Detonations. Combustion Science and Technology, 1, 65.

Mitchner, M. and Kruger, C. H., Jr. (1973). Partially Ionized Gases. John Wiley & Sons, New York.

Miyata, S., Ito, Y. and Shimasaki, Y. (1993). Flame Ion Density Measurement Using Spark Plug Voltage Analysis,.SAE Paper 930462.

Naoumov, V., Demin, A., Andersson, I. and Sokolov, A. (2002). Modeling of Combustion and Non-Equilibrium Ionization in Spark Ignition Engines. SAE Paper Number: 2002-01-0009.

Nair, S., Rajaram, R., Meyers, A.J., Lieuwen, T. C., Tozzi, L. and Benson,K. (2005). Acoustic and ion sensing of lean blowout in an aircraft combustor simulator. AIAA paper 2005-0932.

Reinmann, R., Saitzkoff, A. and Mauss, F. (1997). Local Air-Fuel Ratio Measurements Using the Spark Plug as an Ionization Sensor. SAE Paper Number: 970856.

Saitzkoff, A., Reinmann, R., Berglind, T. and Glavmo, M. (1996). An Ionization Equilibrium Analysis of the Spark Plug as an Ionization Sensor. SAE Paper Number: 960337.

Shimasaki, Y. Kanehiro, M, Baba, S. Maruyama, S., Hisaki, T. and Miyata, S. (1993). Spark Plug Voltage Analysis for Monitoring Combustion in an Internal Combustion Engine. SAE paper 930461.

Tisch, D., Alexander, J. and Soltis, D. (2008). Combustion System Development Using Optical Spark Plug Probes. SAE Paper Number: 2008-01-1074.

Williams, F.W. and Sheinson, R.S. (1974). Onset of Ions in Flames. Combustion Science and Technology, 8, 293.

Yoshiyama, S., Tomita, E. and Hamamoto, Y. (2000). Fundamental Study on Combustion Diagnostics Using a Spark Plug as Ion Probe. SAE Paper Number: 2000-01-2828.

Yoshiyama, S. and Tomita, E. (2002). Combustion Diagnostics of a Spark Ignition Engine Using a Spark Plug as an Ion Probe. SAE Paper Number 2002-01-2838.

Yamashita, K. Karnani, S. and Dunn-Rankin, S. (2009). Numerical Prediction of Ion Current from a Small Methane Jet Flame. Combustion and Flame, 156, 1227.

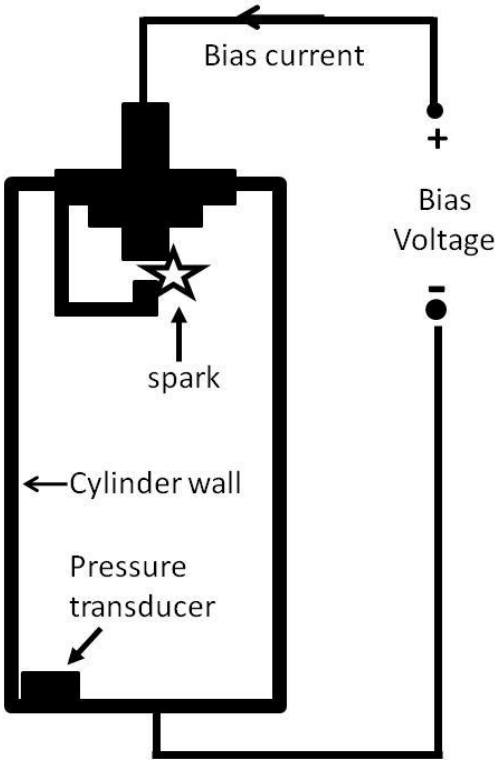

Figure 1: Schematic of constant volume spark-ion probe.

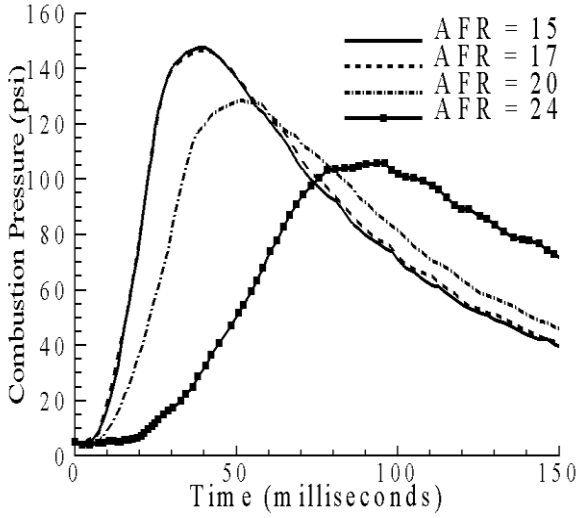

(a)

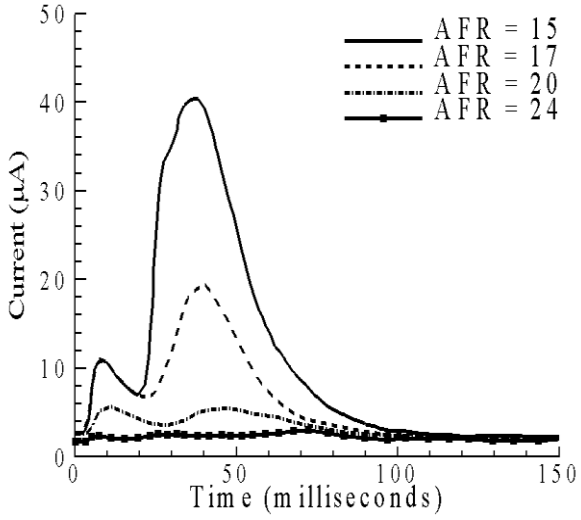

(b)

Figure 2: Temporal variation of cylinder pressure (a) and ion current (b) in a constant volume chamber (An, 1996).

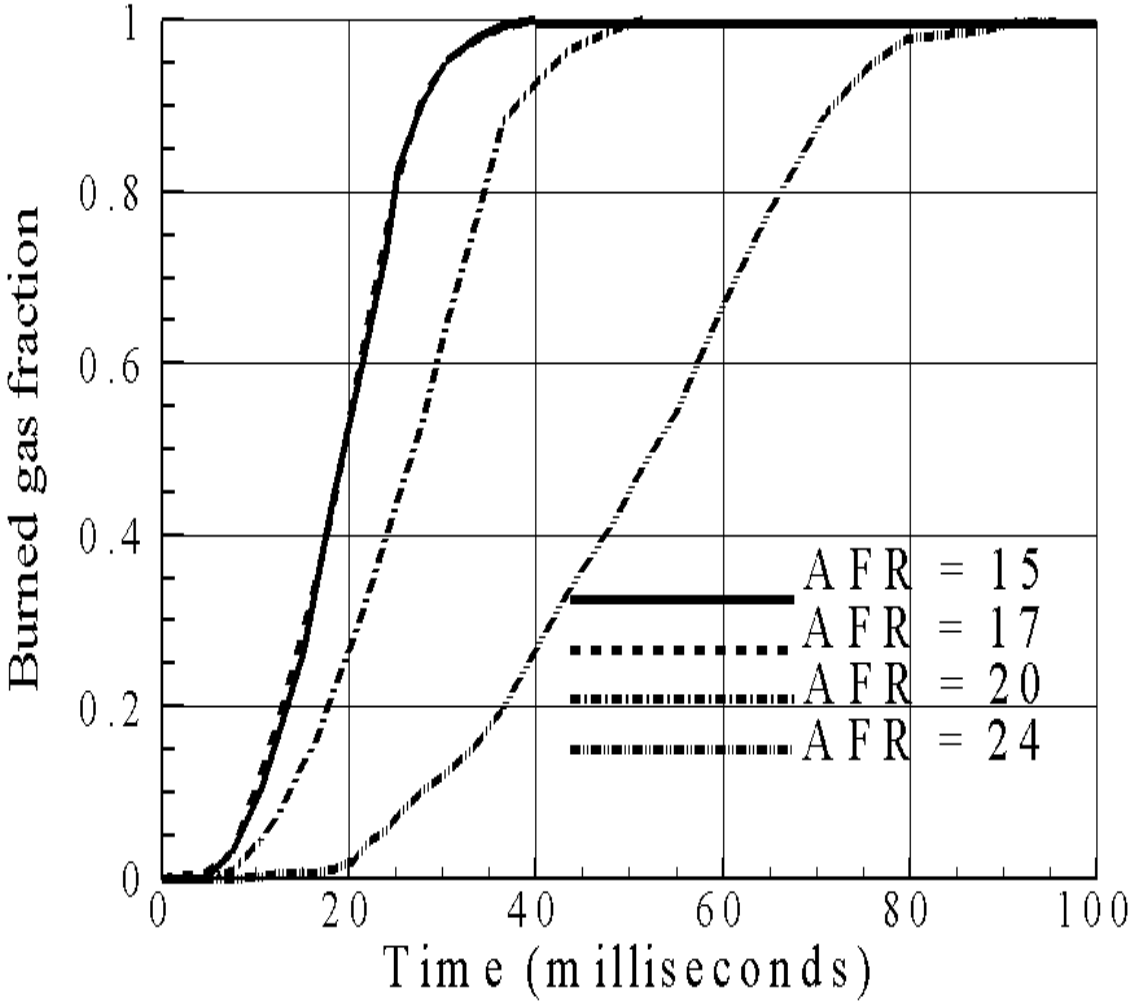

Figure 3: Burned gas fraction for various AFRs.

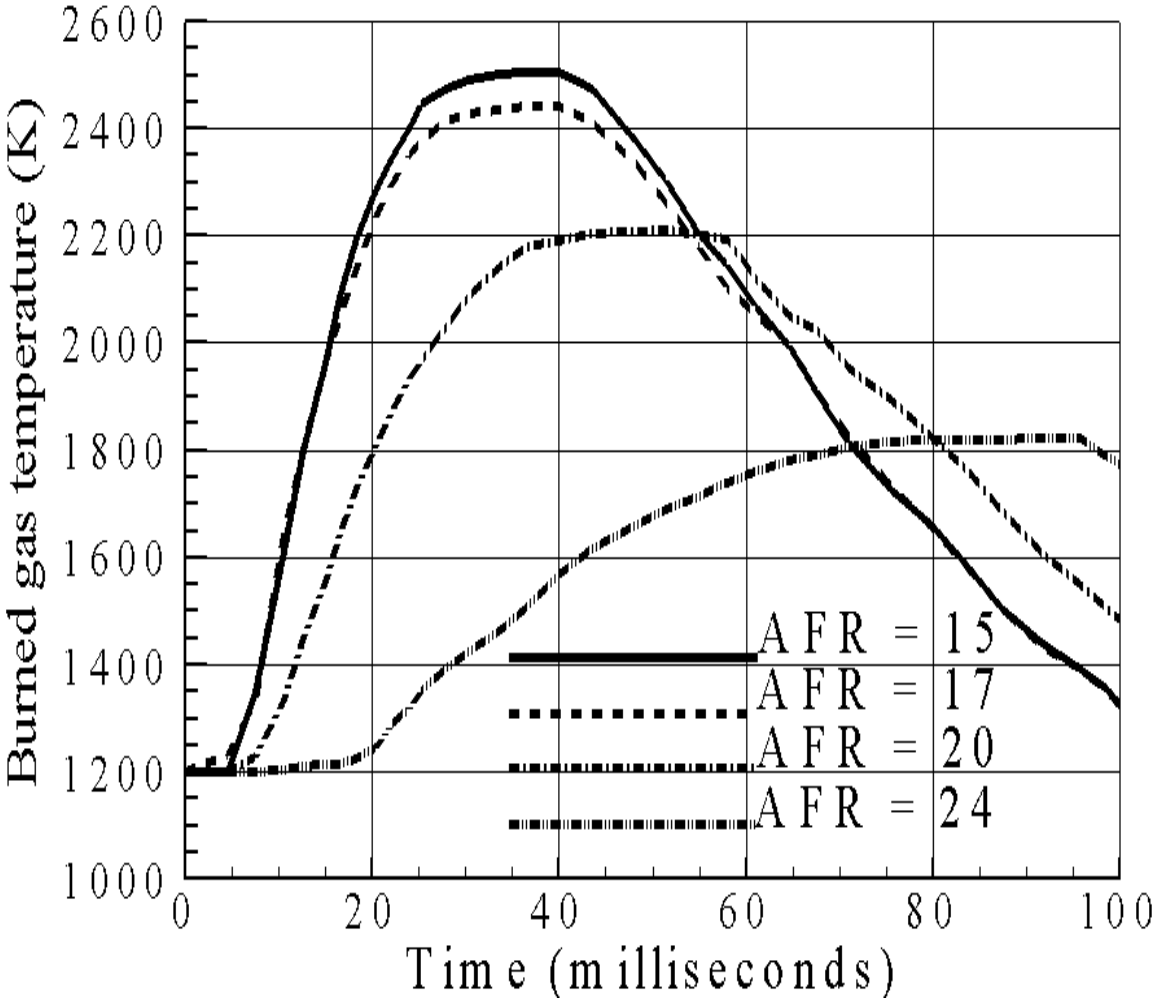

Figure 4: Burned gas temperature for various AFRs.

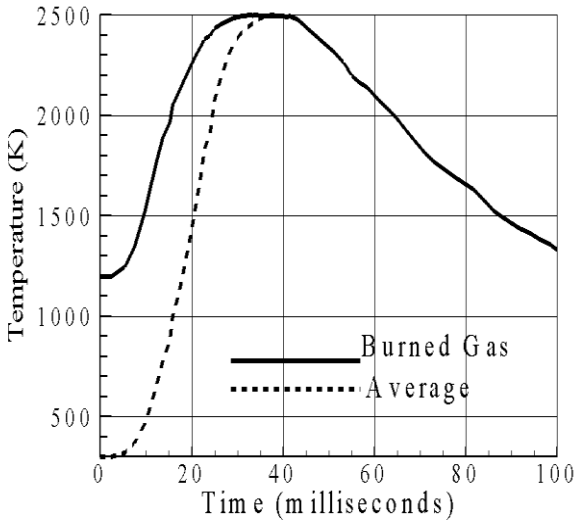

(a)

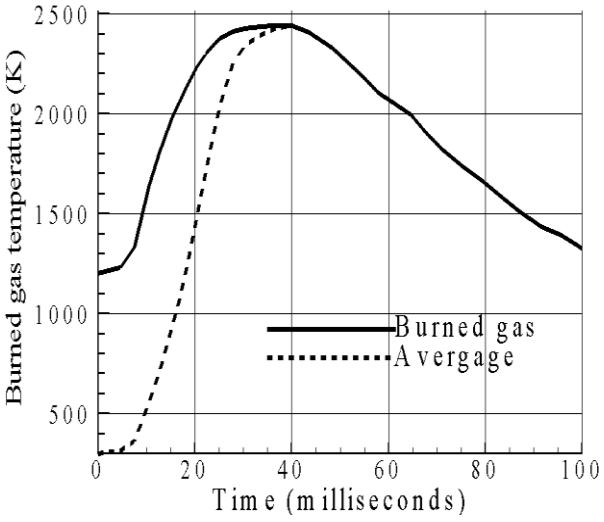

(b)

Figure 5: Burned and average gas temperatures for (a) AFR = 15, (b) AFR = 17

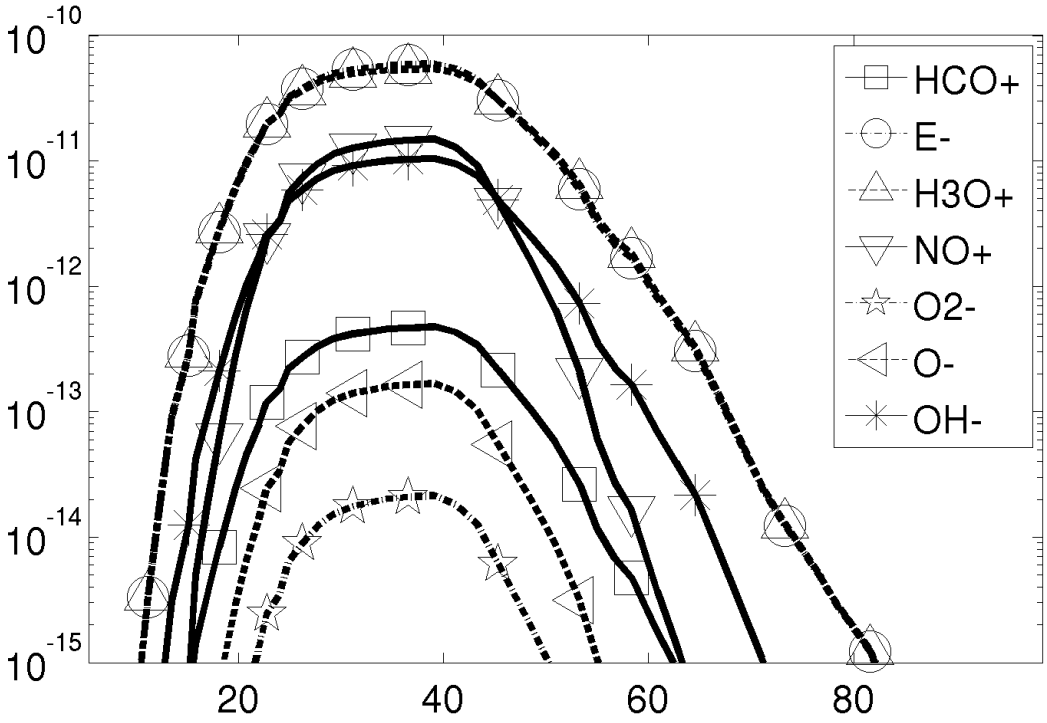

Figure 6 (a): Temporal variation of charged species mole fractions for AFR=15

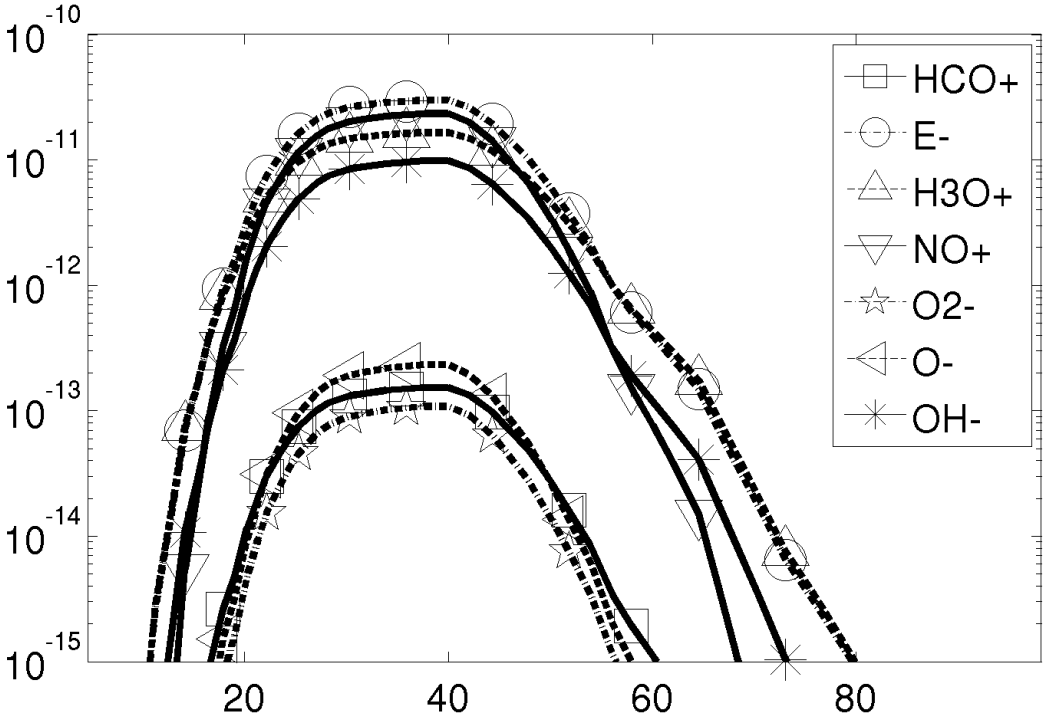

Figure 6 (b). Temporal variation of charged species mole fractions for AFR=17

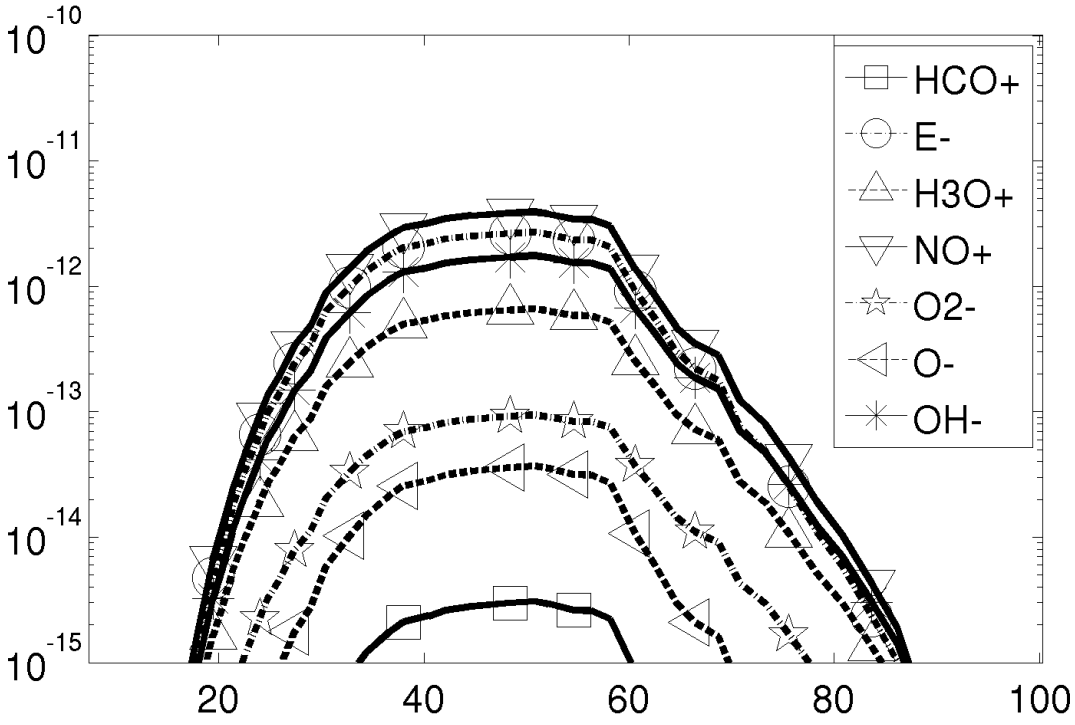

Figure 6 (c): Temporal variation of charged species mole fractions for AFR = 20.

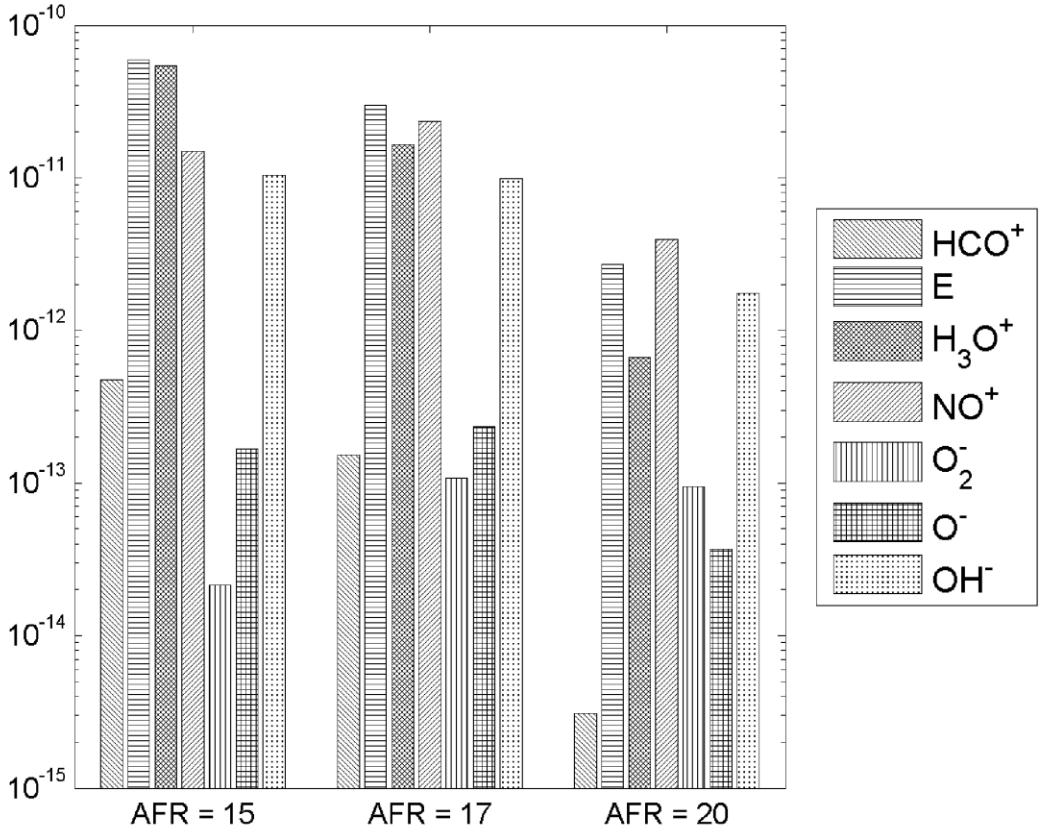

Figure 7: Charged species mole fraction corresponding to the location of peak current for various AFRs.

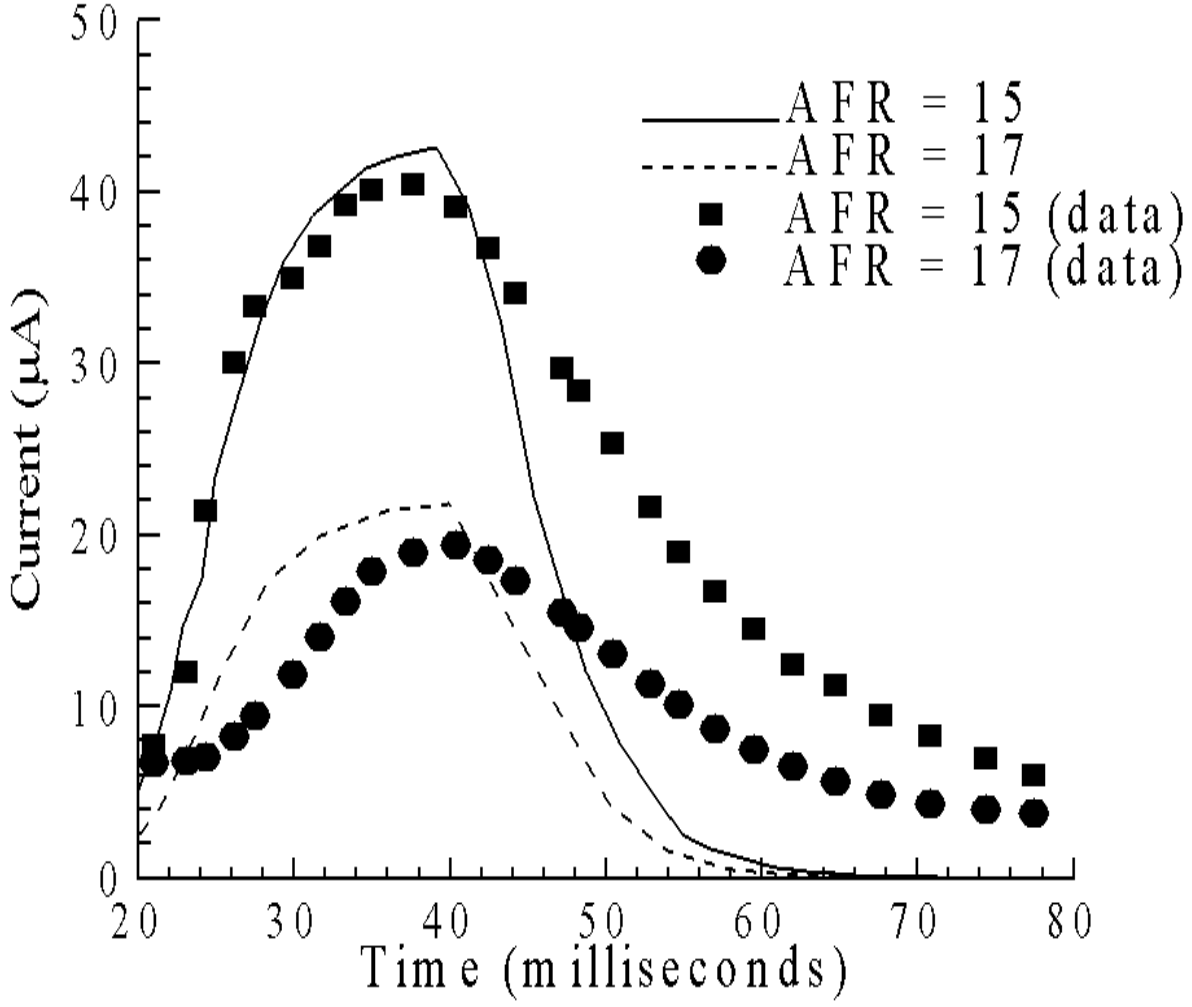

Figure 8: Comparison of current computed by using equilibrium mole fractions of charged-species with experimental data.

Table 1: List of species

	Species
1	CH_4 (fuel)
2	O_2
3	CO_2
4	H_2O
5	N_2
6	N
7	O
8	NO
9	OH
10	H
11	N_2O
12	CO
13	H_2
14	NO_2
15	HO_2
16	CH_3
17	C_2H_2
18	C
19	HCN
20	CH
21	HCO^+
22	e-
23	H_3O^+
24	NO^+
25	O_2^-
26	O^-
27	OH^-

Table 2: List of reactions

1	$\frac{1}{2}H_2 = H$	$k_1 = \frac{[H]}{[H_2]^{0.5}}\sqrt{P}$	$k_1 = 2.5\text{x}10^{-2}$
2	$\frac{1}{2}O_2 = O$	$k_2 = \frac{[O]}{[O_2]^{0.5}}\sqrt{P}$	$k_2 = 1.44\text{x}10^{-2}$
3	$\frac{1}{2}N_2 = N$	$k_3 = \frac{[N]}{[N_2]^{0.5}}\sqrt{P}$	$k_3 = 2.9\text{x}10^{-7}$
4	$\frac{1}{2}H_2 + \frac{1}{2}O_2 = OH$	$k_4 = \frac{[OH]}{[H_2]^{0.5}[O]^{0.5}}$	$k_4 = 0.89$
5	$\frac{1}{2}N_2 + \frac{1}{2}O_2 = NO$	$k_5 = \frac{[NO]}{[N_2]^{0.5}[O]^{0.5}}$	$k_5 = 5.93\text{x}10^{-2}$
6	$H_2 + \frac{1}{2}O_2 = H_2O$	$k_6 = \frac{[H_2O]}{[H_2][O_2]^{0.5}}(P)^{-0..5}$	$k_6 = 168.43$
7	$CO + \frac{1}{2}O_2 = CO_2$	$k_7 = \frac{[CO_2]}{[CO][O_2]^{0.5}}(P)^{-0.5}$	$k_7 = 27.54$
8	$NO + \frac{1}{2}O_2 = NO_2$	$k_8 = \frac{[NO_2]}{[NO][O_2]^{0.5}}(P)^{-0.5}$	$k_8 = 1.77\text{x}10^{-3}$
9	$O_2 + \frac{1}{2}H_2 = HO_2$	$k_9 = \frac{[HO_2]}{[O_2][H_2]^{0.5}}(P)^{-0.5}$	$k_9 = 2.12\text{x}10^{-3}$
10	$N_2 + \frac{1}{2}O_2 = N_2O$	$k_{10} = \frac{[N_2O]}{[N_2][O_2]^{0.5}}(P)^{-0.5}$	$k_{10} = 3.35\text{x}10^{-6}$
11	$CH_4 + 2O_2 = CO_2 + 2H_2O$	$k_{11} = \frac{[CO_2][H_2O]^2}{[CH_4][O_2]^2}$	$k_{11} = 4.2\text{x}10^{16}$
12	$CH_4 = CH_3 + H$	$k_{12} = \frac{[CH_3][H]}{[CH_4]}P$	$k_{12} = 1.49\text{x}10^{-2}$
13	$2CH_3 = C_2H_2 + 2H_2$	$k_{13} = \frac{[C_2H_2][H_2]^2}{[CH_3]^2}(P)$	$k_{13} = 2.1\text{x}10^{6}$
14	$C_2H_2 = 2C + H_2$	$k_{14} = \frac{[C]^2[H_2]}{[C_2H_2]}P^2$	$k_{14} = 2.2\text{x}10^{-12}$
15	$C_2H_2 + N_2 = 2HCN$	$k_{15} = \frac{[HCN]^2}{[C_2H_2][N_2]}$	$k_{15} = 0.41$
16	$CO + OH = CH + O_2$	$k_{16} = \frac{[CH][O_2]}{[CO][OH]}$	$k_{16} = 3.9\text{x}10^{-14}$
17	$CH + O = HCO^+ + e^-$	$k_{17} = \frac{[HCO^+][e^-]}{[CH][O]}$	$k_{17} = 7.11\text{x}10^{-6}$

18	$N + O = NO^+ + e^-$	$k_{18} = \frac{[NO^+][e^-]}{[N][O]}$	$k_{18} = 1.18 \times 10^{-10}$
19	$H_3O^+ + e^- = H_2O + H$	$k_{19} = \frac{[H_2O][H]}{[H_3O^+][e^-]}$	$k_{19} = 6.74 \times 10^{15}$
20	$O_2 + e^- = O_2^-$	$k_{20} = \frac{O_2^-}{[O_2][e^-]} P^{-1}$	$k_{20} = 8.15 \times 10^{-2}$
21	$O + O_2^- = O_2 + O^-$	$k_{21} = \frac{[O_2][O^-]}{[O][O_2^-]}$	$k_{21} = 35.7$
22	$OH + e^- = OH^-$	$k_{22} = \frac{OH^-}{[OH][e^-]} P^{-1}$	$k_{22} = 6.94$

* reaction rates calculated at 2500K